Supplementary Information for

Freestanding interconnected nanocluster textiles for efficient oxygen evolution reaction

Higashi et al.

Corresponding Author: Shougo Higashi (shigashi@mosk.tytlabs.co.jp).

This PDF file includes:

Supplementary Figs. 1-20, Tables 1-4, and refs.1-19

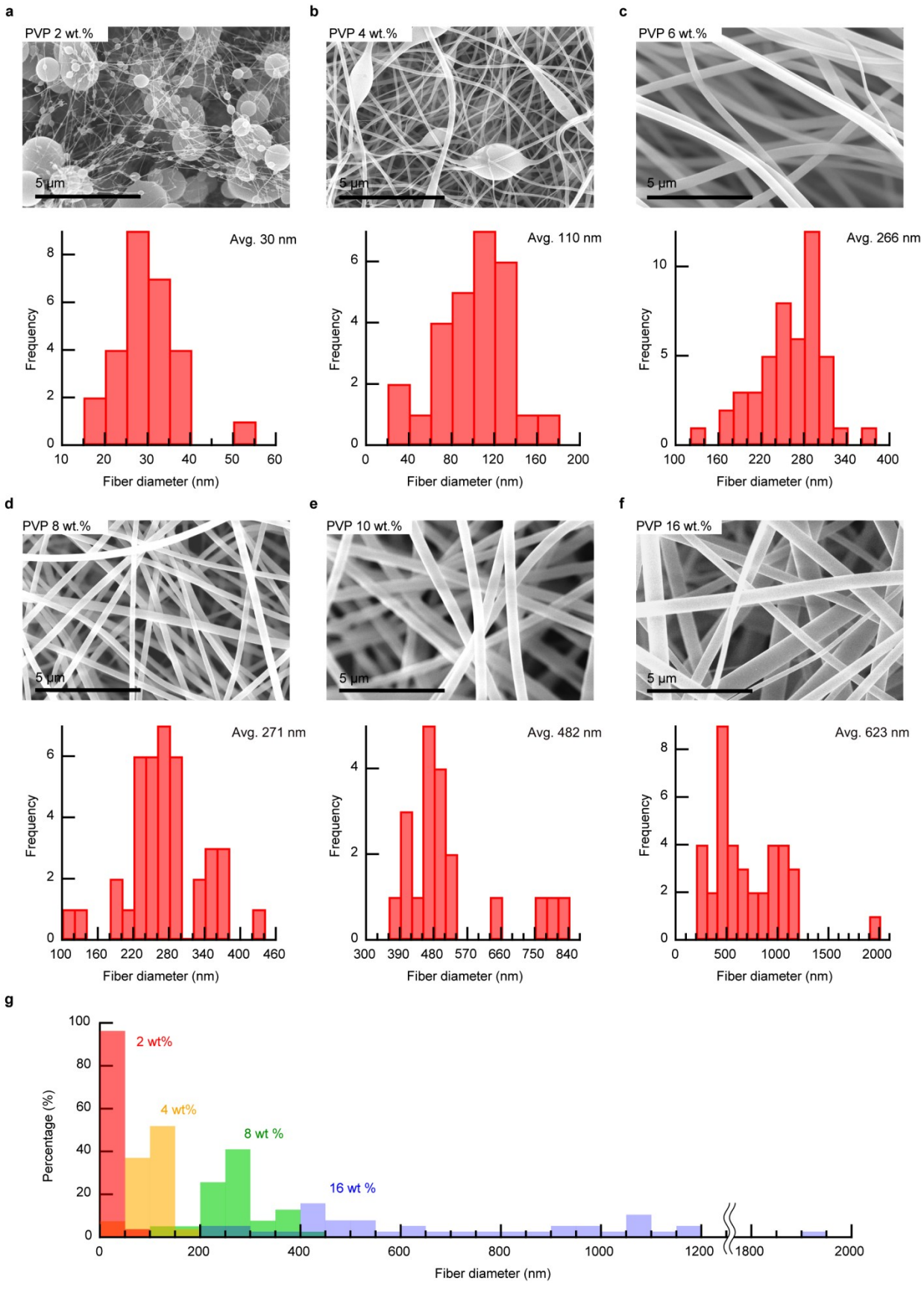
a
PVP 2 wt.%
5 μm
Avg. 30 nm
Frequency
Fiber diameter (nm)
b
PVP 4 wt.%
5 μm
Avg. 110 nm
Frequency
Fiber diameter (nm)
c
PVP 6 wt.%
5 μm
Avg. 266 nm
Frequency
Fiber diameter (nm)
d
PVP 8 wt.%
5 μm
Avg. 271 nm
Frequency
Fiber diameter (nm)
e
PVP 10 wt.%
5 μm
Avg. 482 nm
Frequency
Fiber diameter (nm)
f
PVP 16 wt.%
5 μm
Avg. 623 nm
Frequency
Fiber diameter (nm)
g
2 wt%
4 wt%
8 wt %
16 wt %
Percentage (%)
Fiber diameter (nm)

16

Supplementary Fig. 1: Representative SEM images and fiber diameter distributions of electrospun PVP nanofibers. a, 2 wt.%, **b** 4 wt.%, **c** 6 wt.%, **d** 8 wt.%, **e** 10 wt.%, and **f** 16 wt.% of PVP in methanol solution**.** The PVP concentration is mentioned at the top left of the figure. The average fiber diameter is shown at the top right of the histogram. **g**, Summary of fiber diameter distribution for different concentrations of PVP in methanol solution.

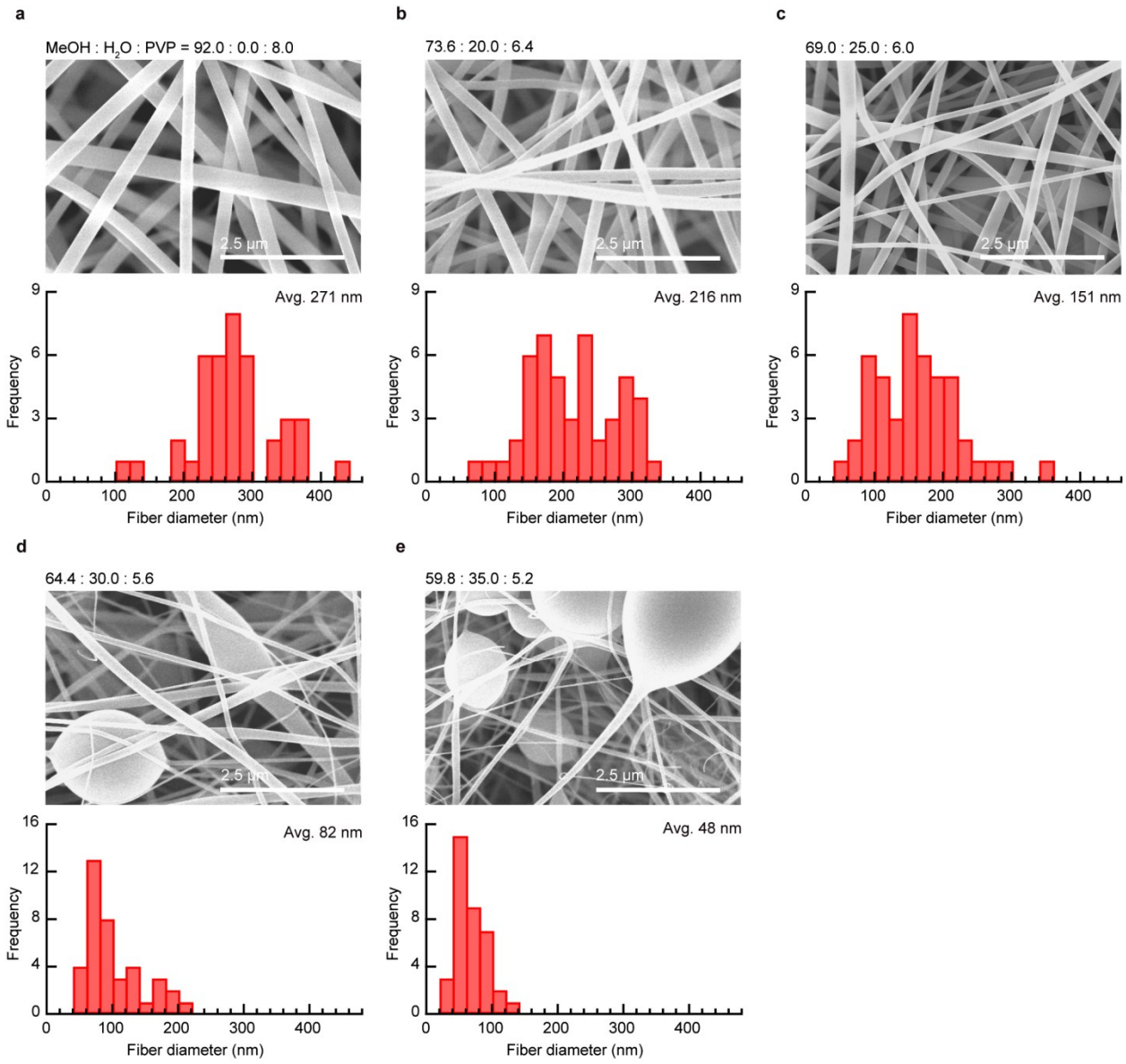

Supplementary Fig. 2: Effect of adding H_2O into methanol solution on fiber diameter and structure. The weight fraction of PVP, MeOH, and H_2O and average fiber diameter are shown at the top left of the SEM image and top right of the histogram, respectively.

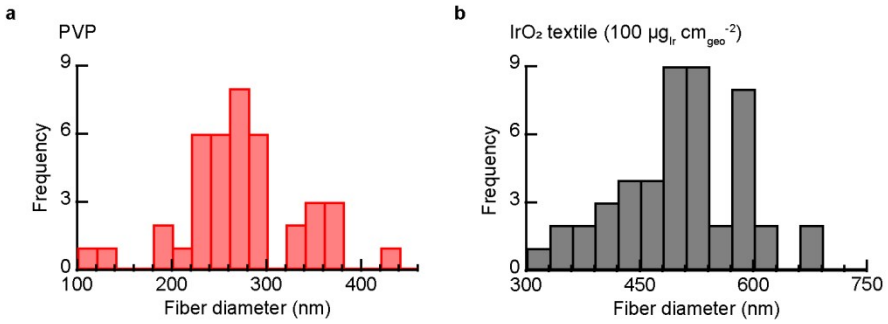

Supplementary Fig. 3: Fiber diameter distributions of IrO_2 textile and pristine electrospun PVP fiber. a, Diameter distributions for pristine electrospun PVP nanofibers and **b**, for IrO_2 textiles (271 nm ID with 100 $\mu g_{\text{-Ir}}$ cm^{-2}).

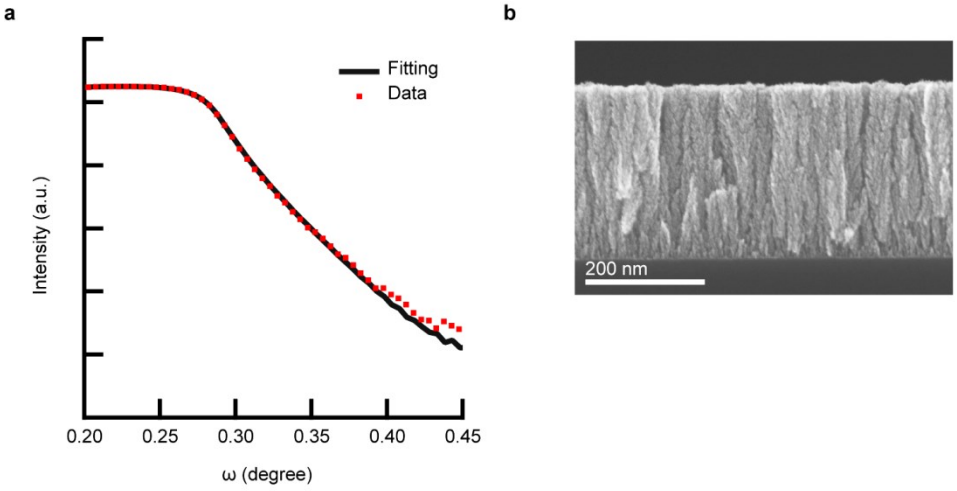

c

IrO_2 Density (g cm^{-3})	4.1
IrO_2 Thickness (nm)	280
IrO_2 surface roughness (nm)	4.88
Si Density (g cm^{-3})	2.32
IrO_2/Si interface roughness (nm)	0.63

Supplementary Fig. 4: IrO_2 film deposited next to the catalyst textile for Ir mass loading estimation. a, XRR curve, **b**, SEM image, and **c**, **the** fitting parameters obtained from the XRR curve of the IrO_2 film deposited on the Si substrate placed next to the catalyst textile during sputtering. The raw data and the fitting curve are represented by the dots and solid line, respectively. The IrO_2 thickness and Si density were fixed parameters. The EDLC of this film was also high over 200 Fg^{-1}, a same level to the IrO_2 textile we prepared in this work. However, the lack of transferability and durability of this film (Fig. 1), which makes it difficult for analyzing the surface of the sample at the atomic level, limits practical application despite high EDLC.

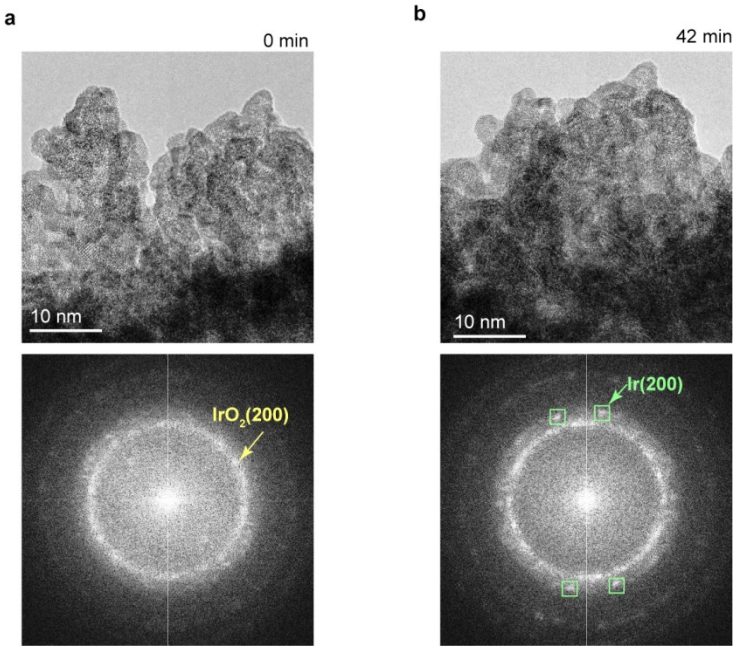

Supplementary Fig. 5: IrO_2 catalyst textile after long-term exposure to the electron beam in TEM. a, TEM image of the IrO_2 catalyst textile immediately after observation and **b**, after 42 min of irradiation. Corresponding FFT images are also shown.

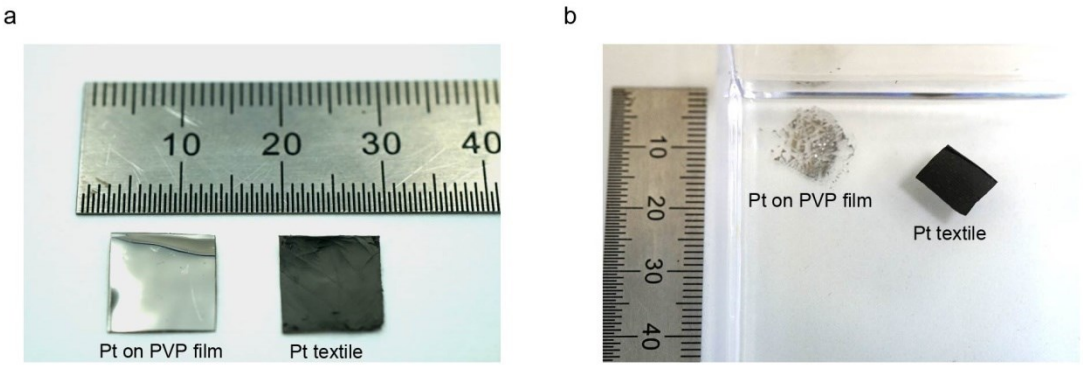

Supplementary Fig. 6: Pt on PVP film and on a nanofiber textile. a, Photograph of Pt on PVP film and on a nanofiber textile before immersion in water and **b,** after immersion into water. While the Pt film disintegrated after immersion, the Pt textile retained its morphology.

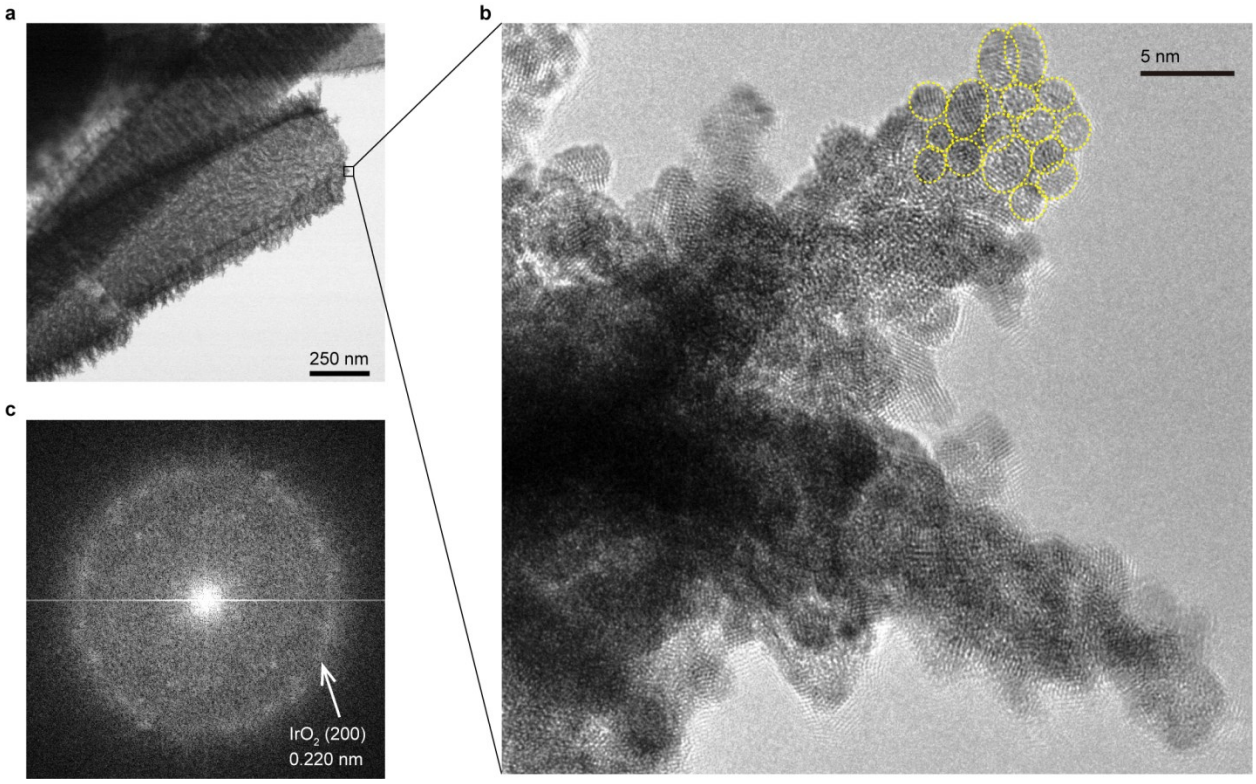

Supplementary Fig. 7: Structure and morphology of an IrO_2 nanocluster textile. **a**, Low-magnification TEM image of a 271 nm ID IrO_2 catalyst textile with mass loading of 100 $\mu g_{\text{-Ir}}\ cm^{-2}_{geo}$. **b**, HRTEM image of the surface of the IrO_2 catalyst textile (the dotted circles outline the nanoclusters, which form a column ~ 5 nm in diameter). **c**, Fast Fourier Transform (FFT) pattern of the TEM image shown in (**b**). The Miller index of the IrO_2 rutile structure estimated from the d-spacing is assigned in the image; these values are consistent with the XRD results (**Supplementary Fig. 3**).

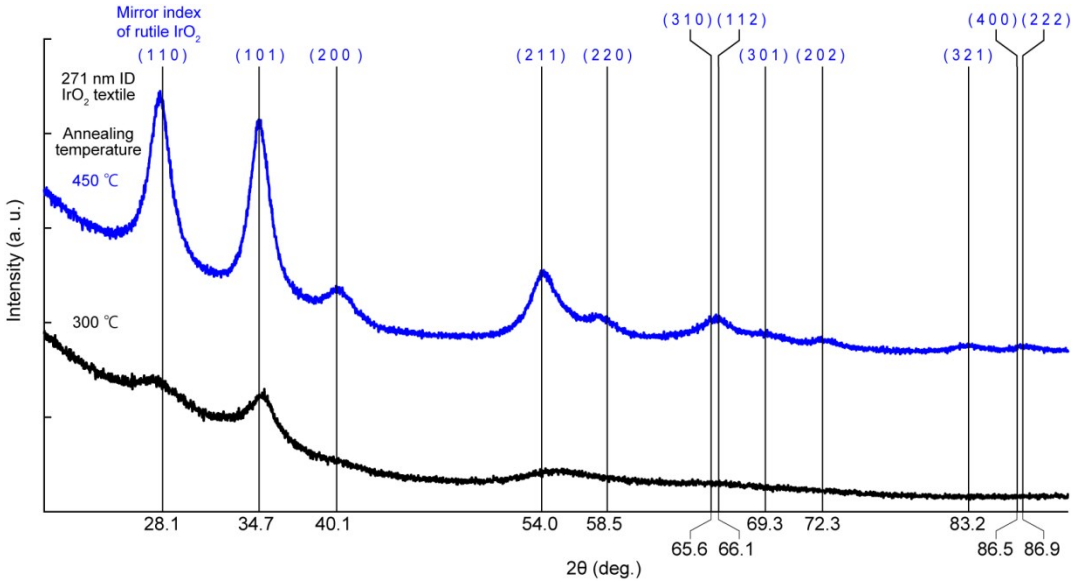

Supplementary Fig. 8: Typical XRD pattern of IrO_2 catalyst textiles. An IrO_2 catalyst textile was prepared by annealing at 300 °C and 450 °C for 10 min. The observed peaks matched with those of rutile IrO_2 (PDF#00-015-0870. See **Supplementary Table 4** for d-spacing).

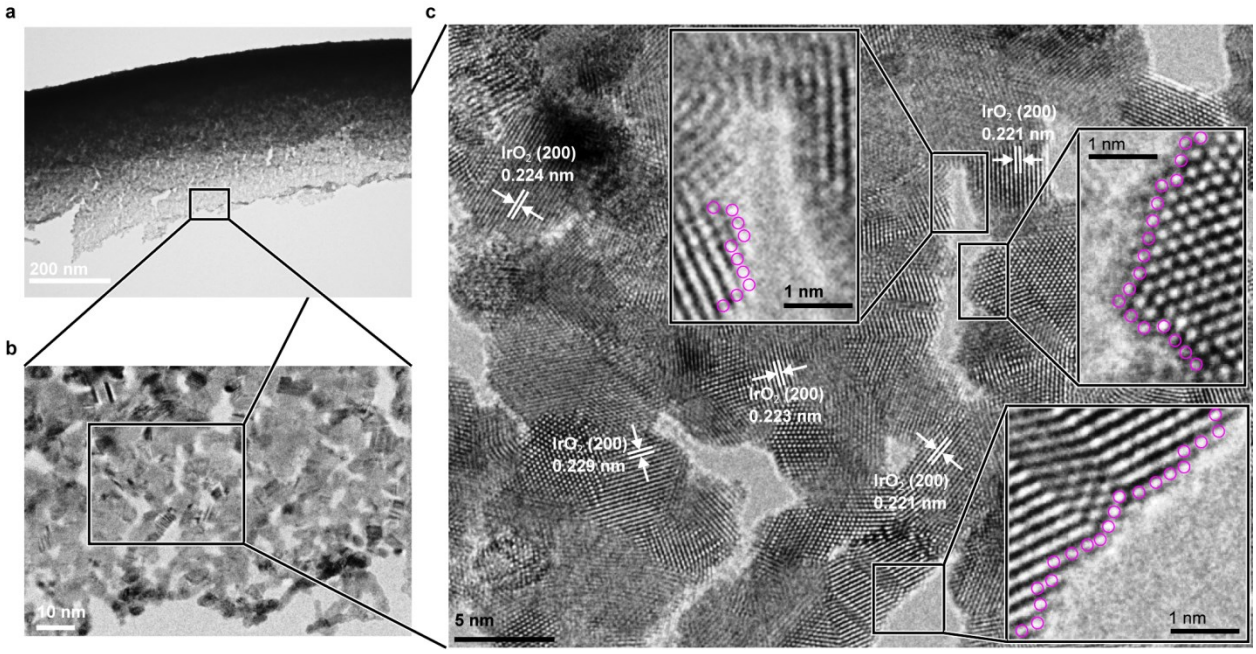

Supplementary Fig. 9: Structure and morphology of an IrO_2 nanocluster textile. a, HR-TEM image of the IrO_2 catalyst textile with a mass loading of 10 $\mu g_{\text{-Ir}}$ cm^{-2}_{geo} annealed at 450 °C. **b,** Magnified image of (**a**). Crystal twinning was clearly observed in (**c**). Surface atoms are marked by circles in the close-up image.

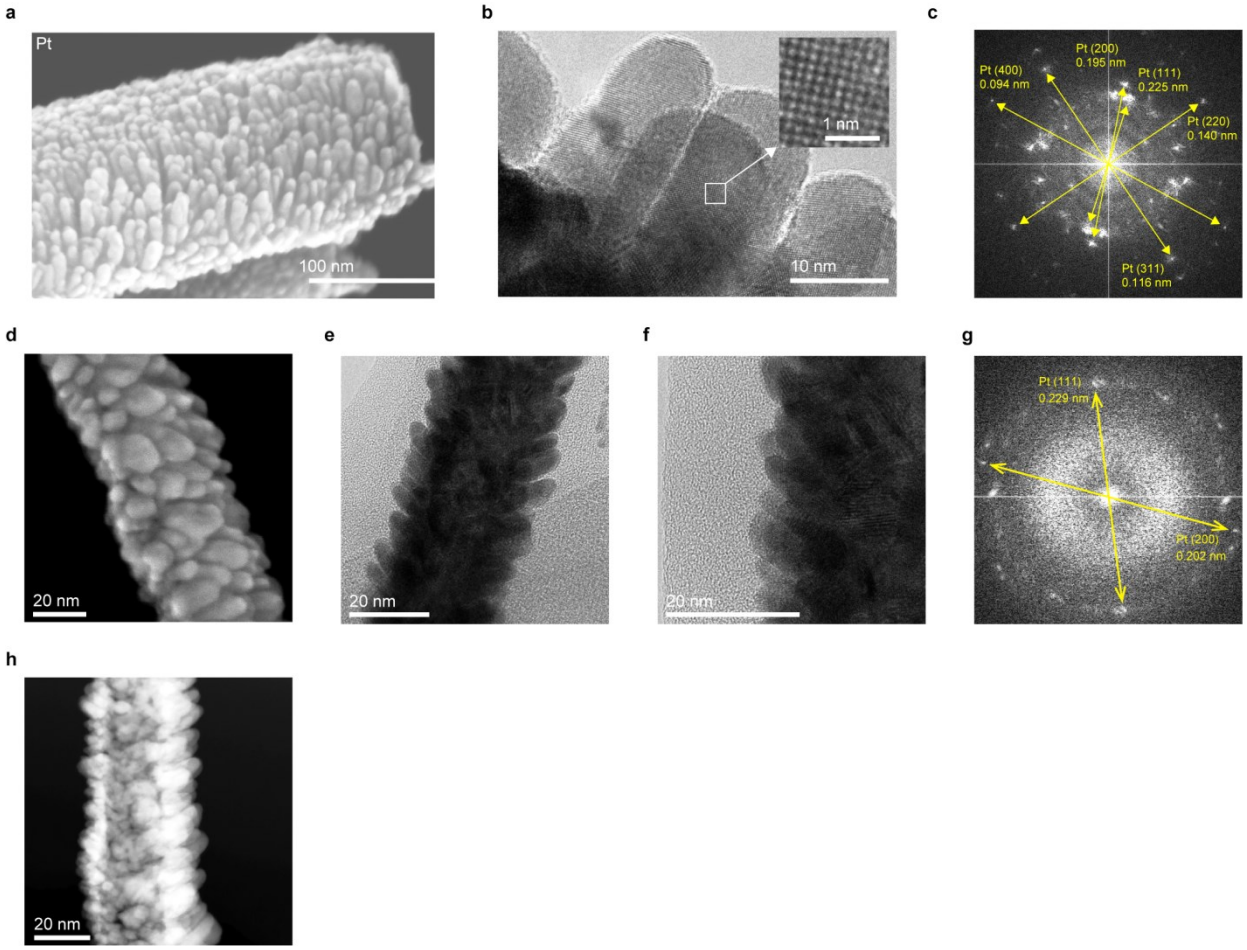

Supplementary Fig. 10: SEM, HRTEM, and FFT images of Pt textiles. a, SEM and **b**, HRTEM image of a Pt nanocluster array formed on a PVP nanofiber prepared using 8 wt.% PVP methanol solution. **c**, FFT pattern of the HRTEM image shown in (**b**). Assigned Miller indices for the diffraction spots of Pt are shown. **d**, SEM, **e**, **f**, HRTEM and **h**, DF-STEM image of the Pt nanocluster array prepared by depositing Pt on a PVP nanofiber prepared using 2 wt.% PVP dissolved methanol solution and **g**, FFT pattern of the HRTEM image shown in (**f**). The Pt textiles were prepared by depositing Pt on the as-prepared electro-spun polymer textiles in a vacuum chamber by magnetron RF sputtering. During sputtering, the pressure was 7 Pa with Ar gas flow.

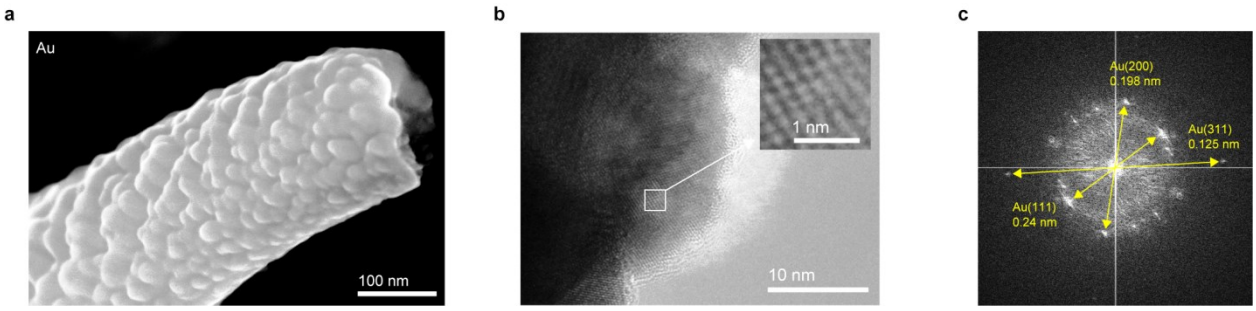

Supplementary Fig. 11: SEM, HRTEM, and FFT images of an Au textile. **a**, SEM and **b**, HRTEM image of Au nanocluster arrays formed on PVP nanofibers made of 8 wt.% PVP solution. **c**, FFT pattern of the HRTEM image shown in (**b**). The Au textile was prepared by depositing Au on the as-prepared electro-spun polymer textiles in a vacuum chamber by magnetron RF sputtering. During sputtering, the pressure was 7 Pa with Ar gas flow.

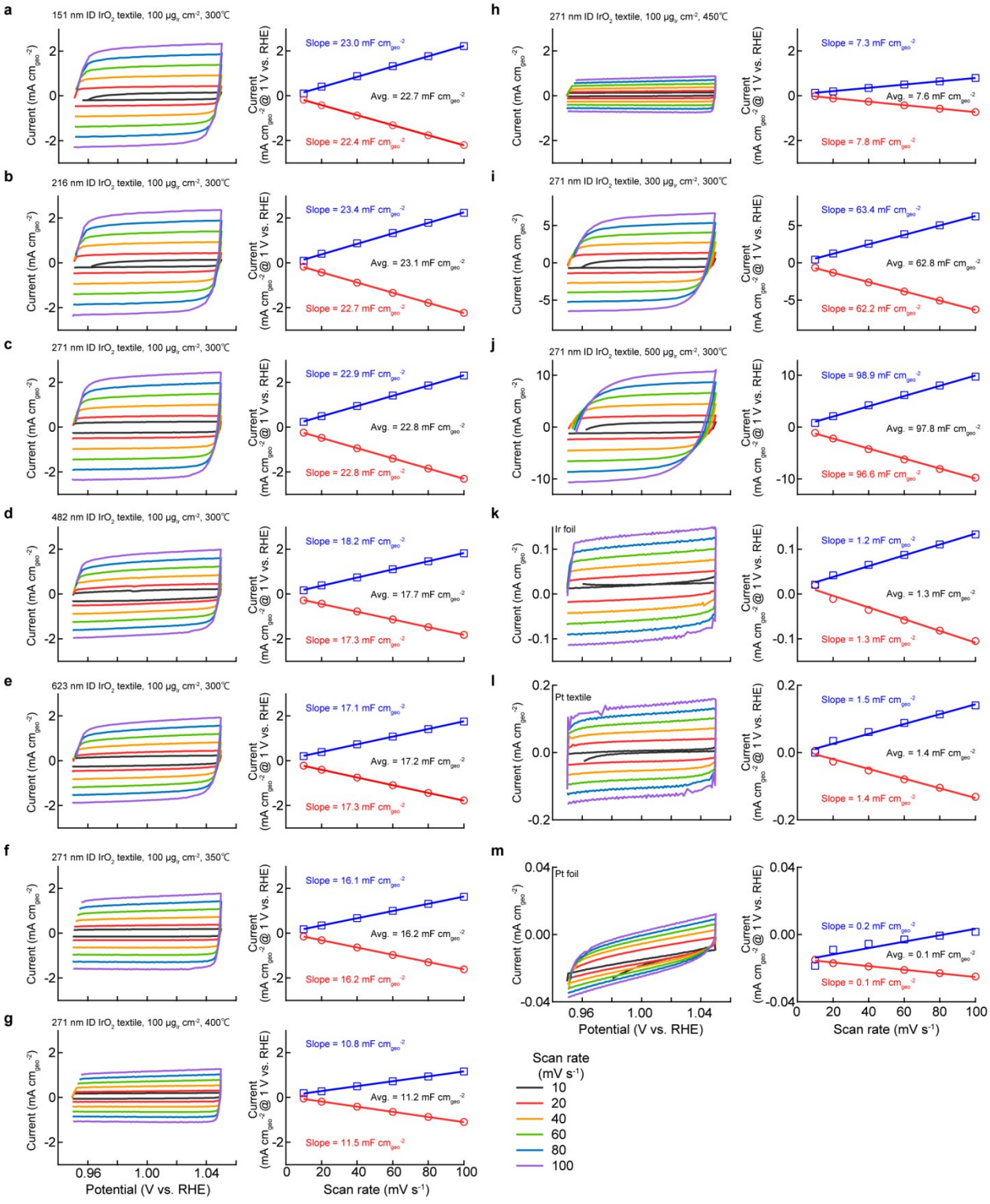

Supplementary Fig. 12: Estimation of electric double-layer capacitance (EDLC) for all of the samples shown in Fig. 3. a-j IrO_2 catalyst textiles with different IDs, mass loadings, and annealing temperatures. **k,** Ir foil, **l**, Pt textile, and **m**, Pt foil. The EDLC is the average of the absolute value of the linear slope fit to the data. To estimate the EDLC, we confirmed the

absence of any noise and faradaic current for the CV at 1.00 V vs. RHE, where we read the anodic and cathodic current. The EDLC values are summarized in **Supplementary Table 2**.

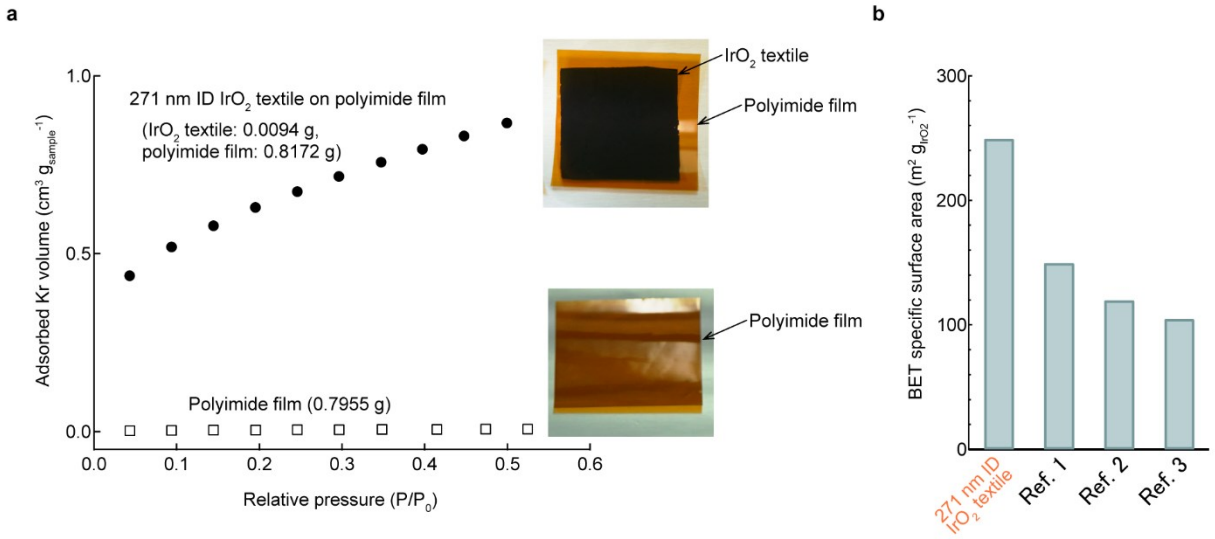

Supplementary Fig. 13: BET characterization of IrO_2 textile. a, Kr adsorption isotherms at −196 °C of IrO_2 textile supported on polyimide film (filled circles). BET surface area was calculated from the linear section of BET plot (P/P_0 = 0.09 - 0.3). 3 × 3 cm^2 IrO_2 textile (271 nm ID) of 100 μg_{Ir} cm^{-2} was transferred onto a 3.5 × 3.5 cm^2 polyimide film (0.05 mm thickness), and then annealed at 300°C for 10 min. Nine of these samples were prepared, cut into 5 × 5 mm^2, and introduced into the BET measurement cell. Total amount of the BET measured IrO_2 textile and polyimide film was 0.0094 g and 0.8172 g, respectively. We confirmed that the BET surface area of polyimide film was negligibly small (open squares). **b**, The BET specific surface area of the IrO_2 textile compared with previous literature for IrO_2 nanoparticle[1, 2, 3].

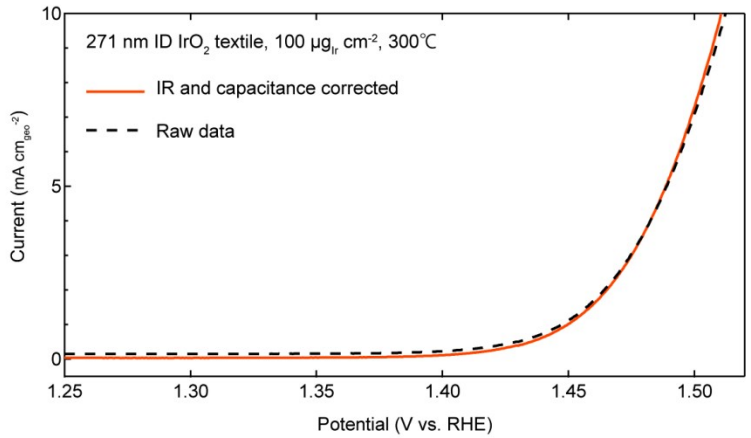

Supplementary Fig. 14: Ohmic and capacitive corrections of the as-measured OER activity of an IrO_2 textile. The as-measured OER activity of the IrO_2 textile ("raw data", dashed black line) is ohmically corrected with the measured ionic resistance of 1.032 Ω. The ohmic-corrected OER current is then capacitance-corrected by taking an average of forward and backward scans (Supplementary Fig. 12c) to yield the final electrode OER activity (solid orange line).

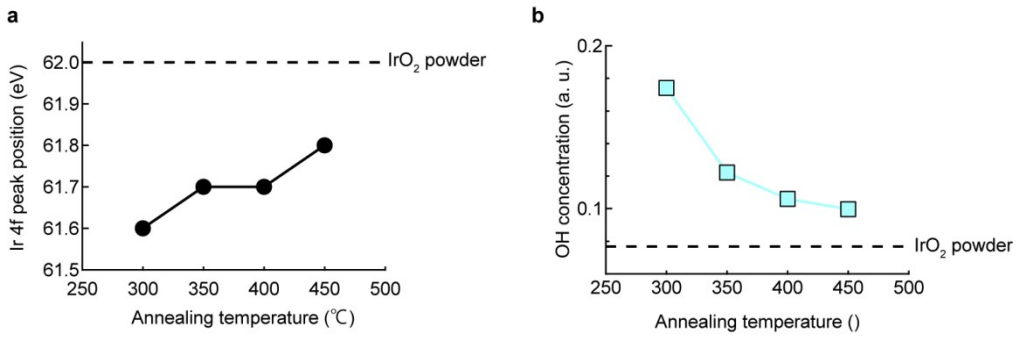

Supplementary Fig. 15: XPS analysis for 271 nm ID IrO_2 catalyst textiles of different annealing temperature (300, 350, 400, and 450 ˚C). **a**, Ir 4f peak position for IrO_2 textile. Dashed line represents peak position for IrO_2 powder. **b**, OH concentration estimated from XPS O 1s spectra (Fig. 5 in the main text). Dashed line represents OH concentration for IrO_2 powder. IrO_2 textiles have a higher OH concentration than IrO_2 powder (**b**). This suggests that the IrO_2 textiles are more reduced, consistent with the lower peak positions of Ir 4f (**a**). Upon annealing, the OH concentration decreased and Ir 4f peak shifts to higher binding energy, indicating oxidization of Ir occurred.

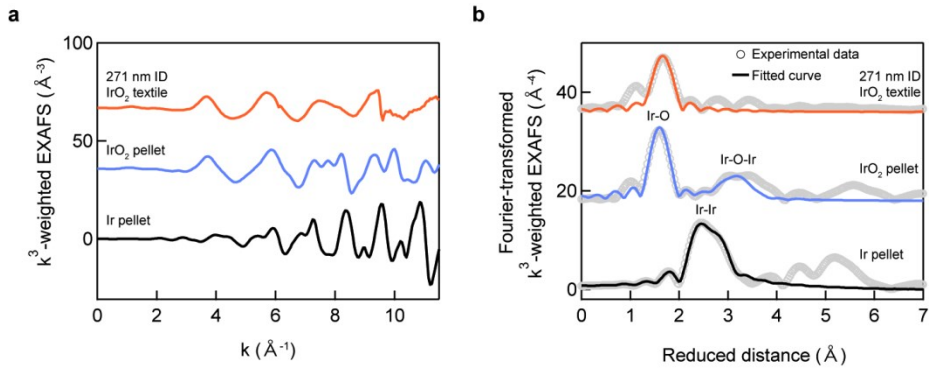

Supplementary Fig. 16: XAFS spectra of the IrO_2 textile. a, k^3-weighted EXAFS spectra of the IrO_2 textile and the control samples of Ir and IrO_2 pellets. Fig. 5d in main text. **b**, Fourier transforms of EXAFS spectra for k = 2.5–11 $Å^{-1}$ and EXAFS simulation. The fitting parameters are summarized in **Supplementary Table 3**.

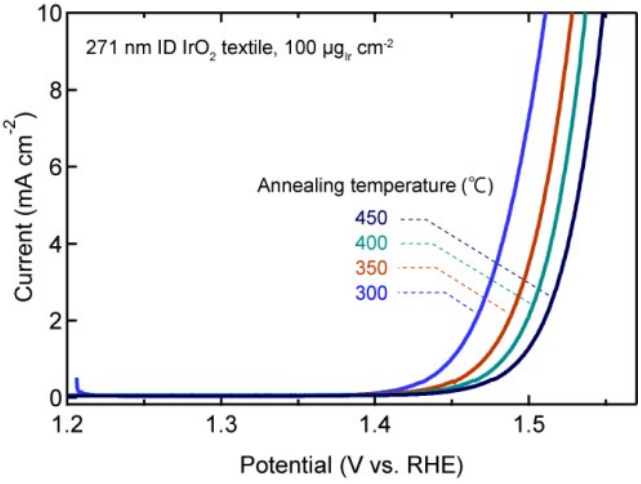

Supplementary Fig. 17: LSV curves of IrO2 textiles annealed at different temperatures. LSVs obtained for 271 nm ID IrO_2 catalyst textiles of different annealing temperature (300, 350, 400, and 450 ˚C). Ir loading is 100 $\mu g_{\text{-Ir}}\ cm^{-2}{}_{geo}$.

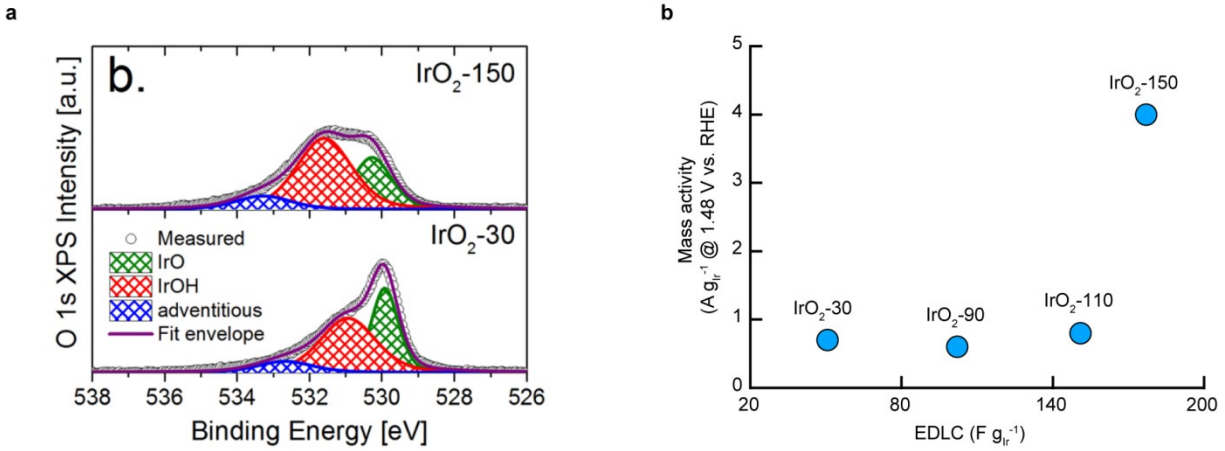

Supplementary Fig. 18: Mass activity of IrO_2 and their XPS spectra from reference [1] **a**, O 1S XPS spectra of different IrO_2 samples from Fig. 4b of Ref. [1]. **b**, Mass activity at 1.48 V vs. RHE with respect to EDLC were calculated and reproduced from Fig. 5a of Ref. [1], showing the higher activity of samples with OH rich surfaces.

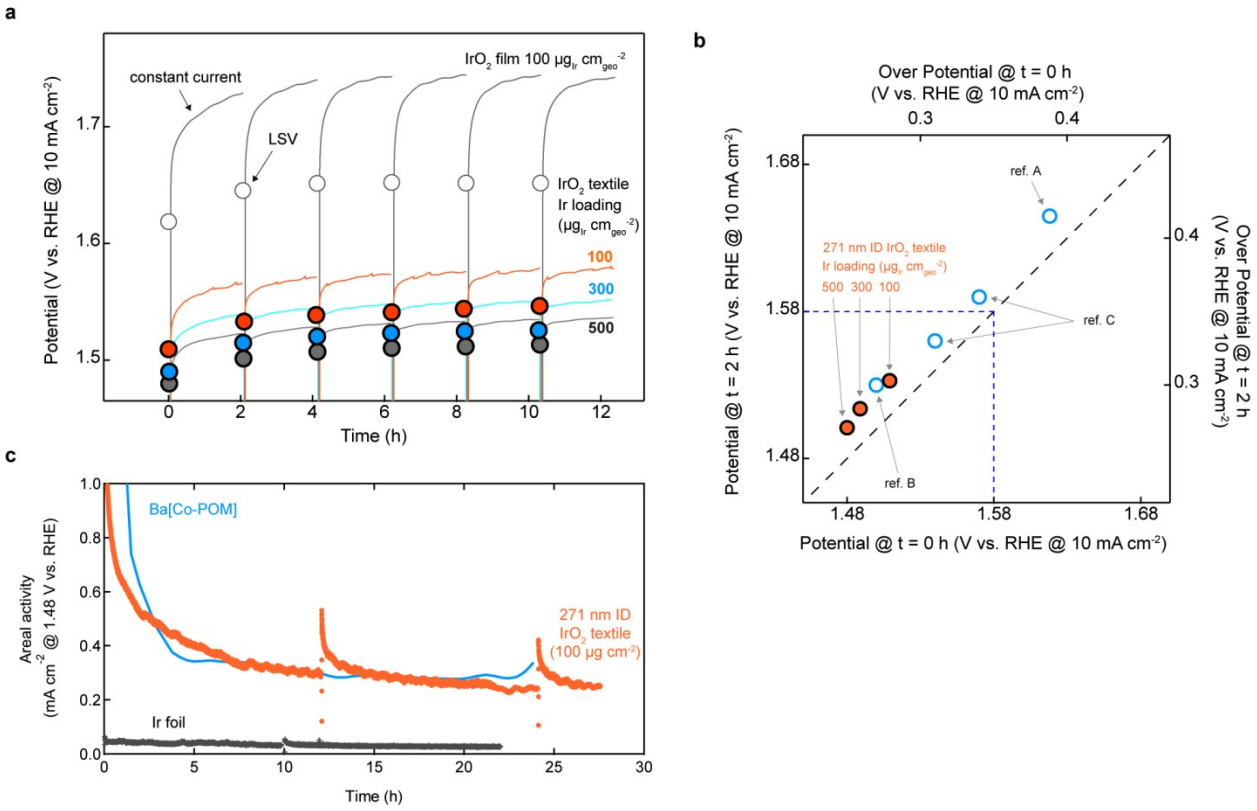

Supplementary Fig. 19: Comprehensive plots of catalytic activity and stability. a, Potential required to reach 10 mA cm^{-2}_{geo} for IrO_2 textiles with different Ir loadings (100, 300, and 500 μg_{Ir} cm^{-2}_{geo} are represented by filled circles, squares and filled squares) and a flat IrO_2 film with Ir loadings of 100 μg_{Ir} cm^{-2}_{geo} (open circles). After linear sweep voltammetry (LSV), a constant current of 10 mA cm^{-2}_{geo} was applied for 2 h and the process was repeated. A constant current produced bubbles and increased the resistivity; thus, the lines connecting the circles for each sample show the intrinsic potentials to IrO_2 textiles. **b**, The change in potential after 2 h of durability testing for IrO_2 textiles with different Ir loadings; the x-axis represents initial overpotential and the y-axis represents overpotential after the 2 h of stability testing. For comparison, the results of previously reported pure IrO_2 catalysts are plotted as blue open circles (A: ref. [4], B: ref. [5], C: ref. [6]). The catalysts that fall within the region surrounded by blue dashed lines are suggested to be practically useful[5, 6]. **c**, Areal activity of a 271 nm ID IrO_2 textile with Ir loading of 100 μg cm^{-2} and Ir foil at a constant overpotential of 250 mV (or 1.48V vs. RHE), compared with the result reported previously for Polyoxometalate electrocatalyst ($Ba_8[Co_9(H_2O)_6(OH)_3(HPO_4)_2(PW_9O_{34})_3]\cdot 55H_2O$) denoted as Ba[Co-POM])[7]. At 12 and 24 h, the test was aborted to measure the impedance and continued until 27.5 h for comparison.

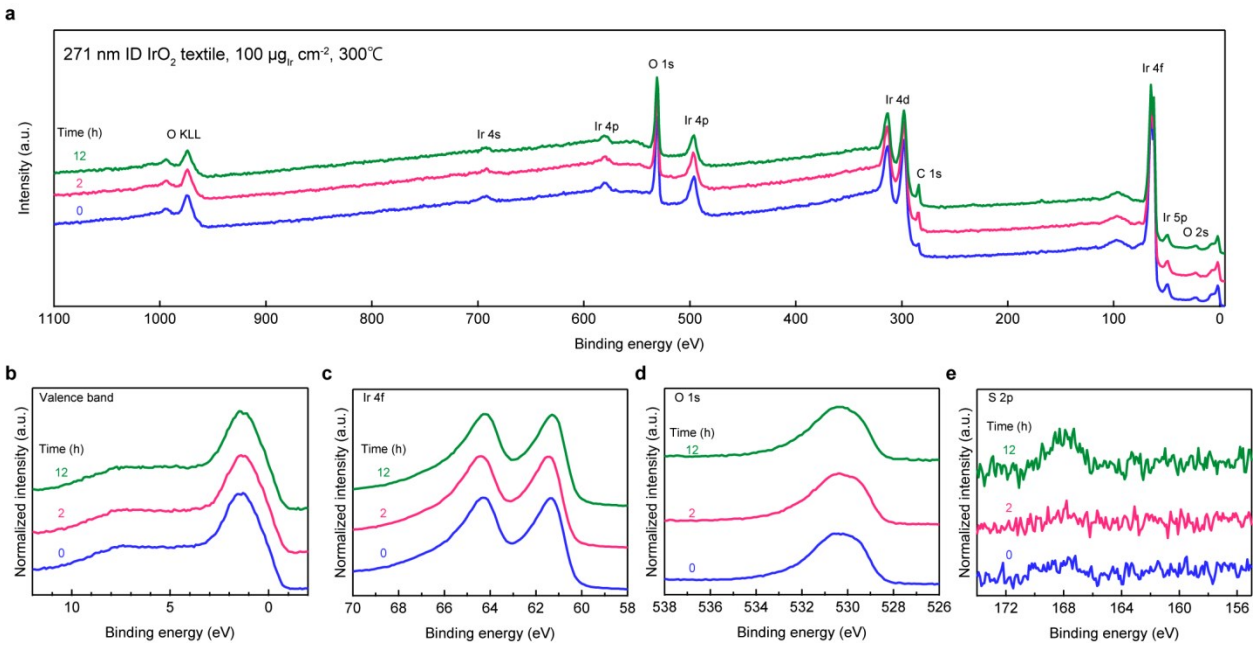

Supplementary Fig. 20: XPS spectra before and after the stability test for 300 ˚C annealed IrO_2 textiles with Ir loading of 100 μg_{-Ir} $cm^{-2}_{geo.}$ a, XPS wide scan results and XPS at valence bands (**b**), Ir 4f (**c**), O 1s (**d**) and S 2p (**e**) are shown. A constant overpotential of 250 mV (or 1.48V vs. RHE) was applied for indicated time in the figures. We observed an increase for S, indicating surface poisoning.

Supplementary Table 1: Summary of the OER activity of pure IrO_2 catalysts

a: Ir loadings were calculated from the catalyst loading and chemical composition. E.g. when the IrO_2 loading is 0.1 mg, the Ir loading is 0.086 mg = 0.1×192 / (192 +32).
b: Calculated using reported electrochemical surface area (ECSA) and 0.627 $mFcm^{-2}$ of the areal capacity of IrO_2 film in 0.5 M H_2SO_4.
c: Calculated using reported ECSA and 0.14 $mFcm^{-2}$ of the areal capacity of polished glassy carbon electrode in 1 M H_2SO_4.
d: Estimated from the average current between 1 to 1.23 V in the CV curve swept at 20 mV s^{-1}.
e: Calculated using reported mass activity and TOF.
f: $Ir(acac)_3$ = Iridium acetylacetonate, $Ir(CH_3COCHCOCH_3)_3$.
g: The values were read from electrochemical measurement data.
h: Estimated from the current @ 1.48 V vs. RHE and anodic charge reported in the literature.
i: Calculated by dividing the current @ 1.48 V vs. RHE by the EDLC (F g^{-1}).
j: Specific activity is defined as the current @ 1.48 V vs. RHE divided by the ECSA. ECSA is defined as the EDLC (mF cm_{geo}^{-2}) of the catalyst divided by 0.035 mF cm_{geo}^{-2}, which is the capacitance of a flat planar electrode in acidic media[5].

Morphology	Ir loading (mg_{Ir} cm^{-2})	EDLC (F g_{Ir}^{-1})	Ir source	Electrolyte	Potential @ 10 mA cm_{geo}^{-2} (V vs. RHE)	Mass Activity @ 1.48 V vs. RHE (A g_{Ir}^{-1})	TOF @1.48 V vs. RHE (s^{-1})	Specific activity @ 1.48 V vs. RHE (μA cm^{-2}_{ECSA}) [j]	Ref.
271 nm ID textile	0.1	228	Bulk Ir metal	0.5 M H_2SO_4	1.51	36	0.159	5.57	This study (See Table S2)
Thin film	–	–	$Ir(CH_3COO)_n$	0.1 M $HClO_4$	1.55 [g]	–	0.020 [h]	0.70	[8]
					1.55 [g]		0.037 [h]	1.30	
					1.6 [g]		–	–	
			$Ir(acac)_3$ [f]	1 M H_2SO_4	1.45 [g]				[9]
					1.56 [g]				
Commercial powder	0.012	158 [b]	–	0.1 M $HClO_4$	–	1.4 [g]	0.009 [i]	0.32	[10]
Nanoparticle with carbon black	0.01	797 [d]	$Ir(CH_3COO)_3$	0.05 M H_2SO	1.51 [g]	23 [g]	0.029 [i]	1.02	[11]
Nanoparticle	0.18 [a]	–	K_2IrCl_6	0.1 M $HClO_4$	1.55 [g]	7.4 [g]	–	–	[12]
	0.77 [a]	124		0.5 M H_2SO_4	1.522	4.2 [g]	0.034 [i]	1.19	[13]
	0.086 [a]	177 [e]	$Ir(acac)_3$ [f]	0.1 M $HClO_4$	–	4.0	0.022 [i]	0.77	[1]
		151 [e]				0.8 [g]	0.005 [i]	0.18	
		102 [e]				0.6 [g]	0.006 [i]	0.21	
		50.6 [e]				0.7 [g]	0.014 [i]	0.49	
	0.043 [a]	116	$IrCl_x{\cdot}yH_2O$		1.67 [g]	3.5	0.030 [i]	1.05	[14]
	0.171 [a]	166	K_2IrCl_6	0.5 M H_2SO	1.527	11.0 [g]	0.066 [i]	2.31	[15]
	0.153	104	$(NH_4)_2IrCl_6$		1.537	4.1 [g]	0.020 [i]	0.7	[16]
	0.214 [a]	334 [c]	–	1 M H_2SO_4	1.58 [g]	–	–	–	[6]
Nanoneedle		295 [c]			1.54 [g]				
Nanoporous architecture	–	–		0.1 M $HClO_4$	1.53 [g]				[17]

Supplementary Table 2: Summary of EDLC and OER activity of IrO_2 catalyst textiles

[a] Calculated by dividing the mass activity (A g_{Ir}^{-1} @ 1.48 V) by the EDLC (F g_{Ir}^{-1}).

				EDLC			OER activity				
Sample	ID (nm)	Annealing temperature (°C)	Mass loading (μg_{Ir} cm^{-2})	Capacitance (mF)	Areal capacitance (mF cm^{-2})	Mass capacitance (F g_{Ir}^{-1})	Potential (V @ 10 mA cm^{-2})	Areal activity (mA cm^{-2} @ 1.48 V)	Mass activity (A g_{Ir}^{-1} @ 1.48 V)	TOF (s^{-1} @1.48 V) [a]	Specific Activity (mA cm^{-2}_{ECSA} @ 1.48 V)
Ir foil	-	-	-	0.25	1.25	-	1.615	0.13	-	0.102	3.57
IrO_2 textile	151	300	100	4.46	22.70	227	1.511	3.45	34.46	0.152	5.32
	216	300	100	4.53	23.09	231	1.510	3.47	34.69	0.150	5.25
	271	300	100	4.48	22.84	228	1.511	3.63	36.35	0.159	5.57
	482	300	100	3.48	17.72	177	1.517	2.54	25.39	0.143	5.01
	623	300	100	3.38	17.21	172	1.522	2.51	25.07	0.146	5.11
	271	300	300	12.33	62.82	209	1.490	7.03	23.43	0.112	3.92
	271	300	500	19.20	97.76	195	1.480	10.08	20.17	0.103	3.61
	271	350	100	3.17	16.17	161	1.528	1.48	14.84	0.092	3.22
	271	400	100	2.19	11.15	111	1.537	0.86	8.61	0.077	2.70
	271	450	100	1.48	7.56	75	1.548	0.53	5.29	0.070	2.45

Supplementary Table 3: Coordination number (N), Debye Waller factor (σ^2), difference in threshold energy (ΔE_0), and Ir-O bond length (R) obtained from nonlinear least-squares curve fits of Fourier transforms of EXAFS spectra.

Sample	Shell	N	σ^2/Å^2	ΔE_0/eV	R/ Å	R-factor
Ir pellet	Ir-Ir	12	0.0026 ± 0.0006	9.09 ± 1.16	2.709 ± 0.005	0.007
IrO_2 pellet	Ir-O	6	0.0008 ± 0.0016	12.99 ± 2.45	1.982 ± 0.012	0.013
	Ir-Ir oxide 1	2	0.0053 ± 0.0153		3.169 ± 0.077	
	Ir-Ir oxide 2	8	0.0087 ± 0.0478		3.602 ± 0.046	
IrO_2 textile	Ir-O	6.06 ± 2.55	0.0031 ± 0.0041	15.96 ± 4.99	2.036 ± 0.028	0.039

Supplementary Table 4: Miller indices and corresponding *d*-spacing of IrO_2 rutile, Ir, IrO_2 pyrite phase, and Pt [18, 19].

IrO_2 rutile		Ir fcc		IrO_2 pyrite		Pt	
hkl	*d*-spacing (nm)	*hkl*	*d*-spacing (nm)	*hkl*	*d*-spacing (nm)	*hkl*	*d*-spacing (nm)
110	0.3178	111	0.2217	111	0.27343	111	0.2266
101	0.2582	200	0.1920	200	0.23665	200	0.1963
200	0.22488	220	0.1357	211	0.19336	220	0.1388
210	0.20119	311	0.1158	220	0.16739	311	0.1183
211	0.1696	222	0.1108	311	0.14270	222	0.1133
220	0.15903	400	0.0960	222	0.13676	400	0.0981
002	0.15771	331	0.0881	321	0.12648	331	0.0901
310	0.14227	420	0.0859	400	0.11837	420	0.0878
112	0.14133	422	0.0784	411	0.11149	422	0.0801
301	0.13542			331	0.10856		
202	0.12914			420	0.10591		
321	0.11604			422	0.09663		
400	0.11247						
222	0.11199						
330	0.10602						
312	0.10563						
411	0.1031						
103	0.1024						
420	0.10058						
213	0.09318						
402	0.09157						
510	0.08822						
332	0.08799						
431	0.08652						
303	0.08609						
422	0.0848						
521	0.08075						
323	0.0804						
440	0.07953						
004	0.07886						

Supplementary References

REFERENCES

1. D. F. Abbott, D. Lebedev, K. Waltar, M. Povia, M. Nachtegaal, E. Fabbri, C. Copéret and T. J. Schmidt, *Chem. Mater.*, 2016, **28**, 6591-6604.
2. S. Song, H. Zhang, X. Ma, Z. Shao, R. T. Baker and B. Yi, *Int. J. Hydrog. Energy*, 2008, **33**, 4955-4961.
3. E. Mayousse, F. Maillard, F. Fouda-Onana, O. Sicardy and N. Guillet, *Int. J. Hydrog. Energy*, 2011, **36**, 10474-10481.
4. T. Tachikawa, A. Beniya, K. Shigetoh and S. Higashi, *Catal. Lett.*, 2020, **150**, 1976-1984.
5. C. C. L. McCrory, S. Jung, J. C. Peters and T. F. Jaramillo, *J. Am. Chem. Soc.*, 2013, **135**, 16977-16987.
6. J. Lim, D. Park, S. S. Jeon, C.-W. Roh, J. Choi, D. Yoon, M. Park, H. Jung and H. Lee, *Adv. Funct. Mater.*, 2018, **28**, 1704796.
7. M. Blasco-Ahicart, J. Soriano-López, J. J. Carbó, J. M. Poblet and J. R. Galan-Mascaros, *Nature Chemistry*, 2017, **10**, 24.
8. T. Reier, D. Teschner, T. Lunkenbein, A. Bergmann, S. Selve, R. Kraehnert, R. Schlogl and P. Strasser, *Journal of the Electrochemical Society*, 2014, **161**, F876-F882.
9. R. D. L. Smith, B. Sporinova, R. D. Fagan, S. Trudel and C. P. Berlinguette, *Chem. Mater.*, 2014, **26**, 1654-1659.
10. F. Godínez-Salomón, L. Albiter, S. M. Alia, B. S. Pivovar, L. E. Camacho-Forero, P. B. Balbuena, R. Mendoza-Cruz, M. J. Arellano-Jimenez and C. P. Rhodes, *ACS Catal.*, 2018, **8**, 10498-10520.
11. H. N. Nong, T. Reier, H.-S. Oh, M. Gliech, P. Paciok, T. H. T. Vu, D. Teschner, M. Heggen, V. Petkov, R. Schlögl, T. Jones and P. Strasser, *Nat Catal.*, 2018, **1**, 841-851.
12. X. Liang, L. Shi, Y. Liu, H. Chen, R. Si, W. Yan, Q. Zhang, G.-D. Li, L. Yang and X. Zou, *Angew. Chem.-Int. Edit.*, 2019, **58**, 7631-7635.
13. L. Yang, G. Yu, X. Ai, W. Yan, H. Duan, W. Chen, X. Li, T. Wang, C. Zhang, X. Huang, J.-S. Chen and X. Zou, *Nat. Commun.*, 2018, **9**, 5236.
14. Y. Lee, J. Suntivich, K. J. May, E. E. Perry and Y. Shao-Horn, *J. Phys. Chem. Lett.*, 2012, **3**, 399-404.
15. J. Chen, P. Cui, G. Zhao, K. Rui, M. Lao, Y. Chen, X. Zheng, Y. Jiang, H. Pan, S. X. Dou and W. Sun, *Angew. Chem.-Int. Edit.*, 2019, **58**, 12540-12544.
16. B. M. Tackett, W. Sheng, S. Kattel, S. Yao, B. Yan, K. A. Kuttiyiel, Q. Wu and J. G. Chen, *ACS Catal.*, 2018, **8**, 2615-2621.
17. Y.-T. Kim, P. P. Lopes, S.-A. Park, A. Y. Lee, J. Lim, H. Lee, S. Back, Y. Jung, N. Danilovic, V. Stamenkovic, J. Erlebacher, J. Snyder and N. M. Markovic, *Nat. Comm.*, 2017, **8**, 1449.
18. Y. Xu, M. Yamazaki and P. Villars, *Jpn. J. Appl. Phys.*, 2011, **50**, 11RH02-11RH02-15.
19. S. Ono, T. Kikegawa and Y. Ohishi, *Physica B: Condensed Matter*, 2005, **363**, 140-145.